Measurement of Ultraviolet Radiative Heating Augmentation in HIEST Reflected Shock Tunnel

Brett A. Cruden[1], Aaron M. Brandis[2]
ERC Inc at NASA Ames Research Center, Moffett Field, CA, 94035

Joseph Olejniczak,[3] Jay Grinstead,[4]
NASA Ames Research Center, Moffett Field, CA, 94035

Lindsay Kirk,[5] Randolph P. Lillard[6]
NASA Johnson Space Center, Houston, TX, 77058

and

Hideyuki Tanno,[7] Tomoyuki Komuro[8]
Kakuda Space Center, Japan Aerospace Exploration Agency (JAXA), Japan, 9811525

Radiance measurements in air at enthalpies from 8-20 MJ/kg have been made over a 250 mm diameter flat-faced test article in Japan Aerospace Exploration Agency's HIgh-Enthalpy Shock Tunnel (HIEST). Measurements were made in the ultraviolet region (200-400 nm wavelength) in an attempt to resolve the long-standing discrepancy between theory and measurements of heat flux over a blunt body; this discrepancy is often attributed to radiation. The spectra obtained indicate the presence of atomic iron vapor in the flowfield. At the highest enthalpies, the radiance is at the blackbody limit. An attempt to model the radiance is made by taking a nominal CFD flowfield without any contamination products and processing it through a line-by-line radiation simulation tool. Iron vapor is introduced into the shocked gas ahead of the model and radiation computations are repeated; the mole fraction of iron vapor is adjusted to match the data. For the higher enthalpy conditions, the radiance was strongly absorbed and it was necessary to adjust the temperature and NO density in the freestream to match the signal below 300 nm. Once the observed spectra were satisfactorily matched, the radiance to the stagnation point was then computed. It is shown that the impurity radiation is sufficiently large to explain the discrepancy.

Nomenclature

H_0	=	Reservoir Specific Enthalpy (MJ/kg)
n_i	=	Number density of species i (cm^{-3})
P_0	=	Reservoir Pressure (MPa)
r	=	Radial distance in facility (cm)
T_{free}	=	Free-stream (vibrational) temperature (K)
x	=	Distance along facility centerline (cm)
x_i	=	Mole fraction of species i

[1] Sr. Research Scientist, Aerothermodynamics Branch. Associate Fellow AIAA. Contact: brett.a.cruden@nasa.gov
[2] Research Scientist, Aerothermodynamics Branch. Senior Member AIAA.
[3] Program Manager, MPCV Aerosciences.
[4] Sr. Research Scientist, Aerothermodynamics Branch. Associate Fellow AIAA.
[5] Aerospace Engineer, Applied Aeroscience and CFD Branch, Member AIAA.
[6] Aerospace Engineer, Thermal Design Branch.
[7] Senior Researcher, Space Transportation Mission Directorate, Member AIAA.
[8] Senior Researcher, Space Transportation Mission Directorate.

y = Distance as measured on spectral image (cm)

I. Introduction

Shock tunnels have long been a preferred method of measuring aeroheating, the magnitude of which drives the selection and sizing of thermal protection systems for vehicles entering planetary atmospheres. Anomalies in heating have been noted in many of these tests, particularly in those conducted in reflected shock tunnels [1-8]. Despite significant efforts, the best available models and correlations are unable to replicate the measured heating magnitudes which are above those expected from theory (or computation). A variety of explanations have been offered for the heating augmentation, including particulate impacts with the surface [8], vibrational excitation/non-equilibrium in the expanded gas [1, 2], boundary layer disturbances [4, 5], model blockage [6], vorticity [7], and radiative heating by heated driver gases [9].

Recent work in the HIEST facility has shown this heating augmentation to scale with the size of the test article and the enthalpy of the gas [3, 10]. By measuring the heat flux through windows on the model surface, it has been shown that most, if not all, of this augmentation can be attributed to non-contact (i.e. radiative) phenomena [11]. Subsequent spectroscopic measurements in the visible to near infrared wavelength range showed the shocked test gas contained impurities that were sufficient to dominate the shock layer radiation, suggesting the radiative heating originated from the shock layer and not the nozzle or further upstream [12]. However, these measurements were not calibrated to absolute units and therefore were not suitable for assessing the radiative heat flux.

In the present work, we report on the measurement of shock layer radiation on a flat face model within the HIEST facility. The data is calibrated in units of absolute spectral radiance and is resolved spatially along the stagnation line and by wavelength from 200-400 nm. The spectra obtained are then fit with the spectral radiance calculated by the NEQAIR code [13], with the level of contamination then used to conduct a wall-directed heat flux calculation. This heat flux is then compared to the experimental heating augmentation.

II. Experimental

A simple flat-faced cylinder (Figure 1) of diameter 250mm was used in the test. This test article was designed to measure the anomalous heat flux augmentation [11]. Two wind-tunnel test campaigns were conducted in JAXA-HIEST [14] shown in Figure 3, the first of which was reported in the paper of Tanno *et al.* [11]. The present work describes the second campaign in which heat flux was measured with reflective thermocouples that are expected to be insensitive to radiative heating. The heat fluxes between the two campaigns are then compared to assess the heating augmentation.

The HIEST facility can be operated at stagnation pressures up to 150 MPa and stagnation enthalpies up to 25 MJ/kg. In the present test campaign, the HIEST contoured nozzle, 2.8 m long with an exit diameter of 800 mm, was used. Calibration of flow in this nozzle is discussed in a previous report [15]. From H_0 = 3.5 MJ/kg to H_0 = 20 MJ/kg, the nozzle calibration tests showed that a steady test core flow diameter prevailed up to 400 mm, in which the deviation of the free-stream Pitot pressure was less than 6%. The test time depends on the stagnation condition – at low-enthalpy conditions (H_0 = 3.5 MJ/kg) the test time is roughly 7 ms, and at high-enthalpy conditions (H_0 = 25 MJ/kg) it is roughly 2 ms. The stagnation condition in this test campaign covered a range of enthalpies (H_0 = 4 to 22 MJ/kg) and the stagnation pressure was around P_0 = 50 MPa. The nozzle reservoir conditions are calculated by an equilibrium code [16] and used as inputs to the Computational Fluid Dynamics (CFD) simulations (described in Section III).

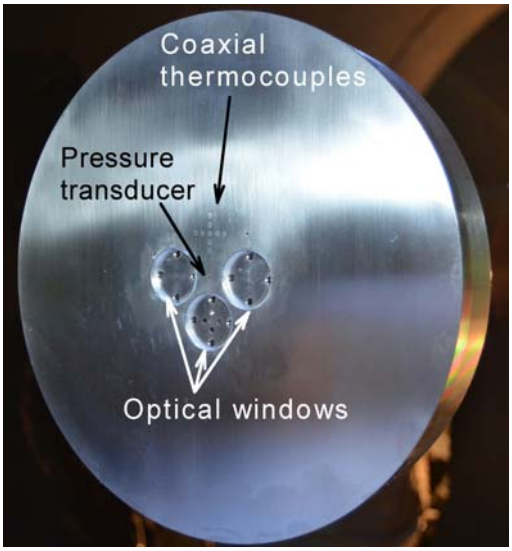

Figure 1. Flat-faced test model. Thermocouple instrumentation can be seen on the model surface.

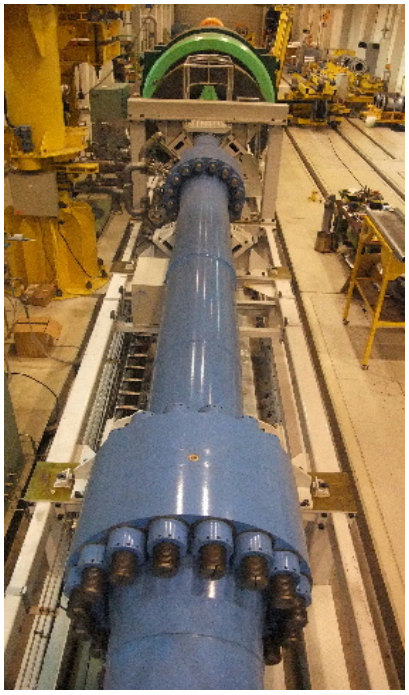

Figure 3. Shock tube and inertia mass of the free-piston shock tunnel HIEST.

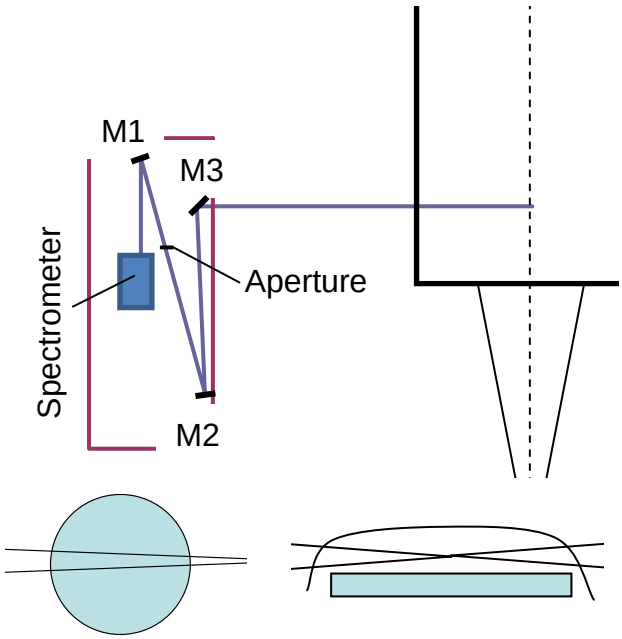

Figure 2. (top) Spectroscopic Path/Layout, (bottom) approximate imaging volume with respect to the test article, (left) front view, (right) top view

The optical set up consists of a McPherson 218 spectrometer with a 246.16 lines/mm grating with 226 nm blaze and PI-Acton PI-MAX2 intensified CCD array with VUV intensifier. The shock in front of the test article is imaged onto the spectrometer by a 4-f optical design that is conceptually similar to that in use in the Electric Arc Shock Tube facility at NASA Ames [17]. This telecentric design is chosen in order to maximize spatial resolution, which is otherwise degraded as the imaging optics cross the shock volume at off-normal angles. This layout, shown in Figure 2, uses two focusing mirrors, M1 and M3. M2 is a flat mirror used to contain the optics within available table space. The focusing mirrors are situated with the spectrometer at the focus of M1 and the test location at the focus of M3. The light between M1 and M3 is therefore collimated. In order to obtain the optimum spatial resolution, the distance between the two mirrors must equal the sum of their focal lengths. The magnification of the image is given by the ratio of M1 to M3. For this test, the working distance of M3 was limited by the size of the test cabin and physical lay out of the facility to be larger than 3.25 m. In order to image a length of 5 cm (slightly longer than the shock stand-off distance) onto the 1.8 cm long axis of the CCD, a de-magnification of 3× is required, and the focal length of M1 must be 1 m or more. This means the total optical path length must be larger than 8.5 m. In order to constrain this length, it was necessary to place the mirror M3 at a right angle at the closest possible location. This results in significant astigmatism, with the sagittal focus being twice the tangential focus. Since it was desired to image the shock tube axis, the mirror was sized with the centerline being the tangential focus. Lack of focus in the sagittal direction was deemed acceptable, as it would be realized as a volume averaging of the shock radiance perpendicular to the centerline. This is displayed in the lower half of Figure 2, which shows the measurement volume of the optics for a single point on the CCD array. The volume of the polyhedron is controlled by the F/# of the optics, which is set by adjusting a variable aperture located at the crossing of off-normal beams between M1 and M2. The width of this aperture was adjusted so that the imaging area at the centerline was 25.4 mm tall. The final optical design utilized a 4.5 m focal length mirror for M3 and 0.914 m focal length for M1. The angles of the mirrors caused their effective (tangential) focus to be 3.26 and 0.906 m, respectively. The mirrors were 254 mm and 152.4 mm diameter, respectively, though this turned out to be oversized given the F/# of 10.8 set by the aperture. Based on this F/#, the diameter of the imaging volume at the shock edge, approximately 125 mm from the focal point, will be 11.6 mm.

Calibration was performed with two sources, a 150mm integrating sphere (LR-C) from Labsphere, LLC, and a laser driven Xenon light source from Energetiq (EQ-1500). The former source was masked to a 25.4 mm × 25.4 mm area to match the optical measurement area and was translated over the centerline to obtain a full field calibration. The integrating sphere has a NIST-traceable calibration in spectral radiance above 300 nm, and was used to obtain the spectrometer calibration in this wavelength range. The EQ-1500 is effectively a point source, and

was measured at three locations along the centerline. The EQ-1500 has been calibrated at the BESSY synchrotron in spectral intensity from 166-410 nm. The intensity measured on the EQ-1500 was scaled to overlap the integrating sphere calibration and then used to extend the wavelength calibration down to 190 nm. Below 190 nm, absorption by ambient oxygen was too great to allow reasonable measurement intensities. The integrating sphere calibration was significantly impacted by scattered light within the spectrometer. Most of the scattered light could be removed by performing a second calibration measurement with a 415 nm long pass filter in front of the spectrometer. The intensity measured with this filter in place was subtracted from the intensity without it. A scaling factor of 1.15× on this measurement was required to remove all signal below the lower limit of the source. An additional correction was made by measuring the instrument lineshape and convolving it with the reference calibration spectrum. This convolved spectrum was used as the normalizing factor to obtain calibration in units of counts per spectral radiance. This calibration factor was then obtained across the entire CCD above 300 nm. Below 300 nm, the spatial dependence was based on the integrating sphere calibration and the wavelength dependence is derived from the EQ-1500 calibration. Polynomial fits of the two dependencies were performed to produce a smooth calibration function.

As the CCD array and spectrometer combination spans about 70 nm, three spectral ranges between 190-400 nm were characterized. The facility was operated at four enthalpy levels from 4-20 MJ/kg. Table I shows the wavelength ranges tested for each nominal enthalpy, along with the calculated nozzle reservoir and freestream conditions. The 4 MJ/kg condition was intended solely for facility check out and ran at 24 MPa. Only one measurement was made at this condition. Due to limitations in facility availability, only two wavelength ranges were measured at 8 MJ/kg. At 14 and 20 MJ/kg, three tests were performed at each enthalpy to cover the majority of radiation from 190-400 nm.

Table I. Summary of test conditions. Nozzle reservoir conditions (except temperature) are measured, while freestream conditions are computed by the DPLR CFD code.

Nominal Enthalpy (MJ/kg)	Nozzle Reservoir Condition			Freestream Condition				Experimental Wavelength Range (nm)
	Enthalpy (MJ/kg)	Pressure (MPa)	Temp. (K)	Velocity (m/s)	Density (kg/m^3)	Trans. Temp. (K)	Vib. Temp. (K)	
4	4.45	24.06	3475	2717	0.0263	315	475	240-310
8	7.96	53.51	5225	3703	0.0284	820	827	240-310
	7.87	56.25	5196	3675	0.0299	801	807	330-400
14	14.22	48.23	7626	4778	0.0157	1525	1530	190-260
	13.32	52.12	7363	4649	0.0179	1457	1462	240-310
	13.83	49.14	7510	4712	0.0166	1602	1608	330-400
20	19.62	45.88	8886	5504	0.0115	1941	1946	190-260
	20.83	47.24	9119	5648	0.0116	2247	2250	240-310
	21.59	47.44	9250	5748	0.0110	2112	2117	330-400

III. Computational

Flow parameters for each of the test runs were predicted computationally with the DPLR v4.02.2 [18] finite volume Navier-Stokes compressible flow solver. The expansion through the nozzle and the flow around the flat plate test article were modeled separately for simplicity. The centerline from the nozzle simulation is extracted and used as the boundary condition for the test article. This approach is supported by the experimental characterization of a 400 mm uniform core flow in Ref. [15]. All solutions were run axisymmetrically and used the same physical models. The flow was modeled with an 11-species air chemistry model, including thermal and chemical non-equilibrium with finite rate chemistry. Transport properties were modeled with the Gupta parameterization of collision integrals [19] and the Yos mixing rule [20] for a multi-species flow. Diffusion coefficients were determined using the Self-Consistent Effective Binary Diffusion (SCEBD) model [21]. The wall boundary condition for both the nozzle and probe test article simulations was assumed to be a non-catalytic, isothermal wall at 300 K. Since the nozzle flow is turbulent and the core is uniform, the wall boundary condition is not expected to impact the core significantly. For the test article, the impact of catalycity was not expected to be large due to the high test pressure, though this assumption was tested and discussed below.

A grid resolution study on the nozzle grid found 178 cells in the axial direction and 600 cells in the radial direction, for a total of 105,000 cells, to be well-converged. CEA (Chemical Equilibrium with Applications)[22] was used to determine the equilibrium chemical composition for the provided stagnation pressure and temperature to be used at the nozzle inflow. Due to the long run length of the nozzle, fully turbulent flow was assumed using the Shear Stress Transport (SST) turbulence model [23]. Computations were also performed using the Spalart-Allmaras

(SA) turbulence model [24], but results showed negligible differences in the freestream conditions at the model location. A sample nozzle solution can be seen in Figure 4 with the log of pressure shown on the top and the translational temperature on the bottom. The black circle indicates the assumed test article location. The nozzle centerline results, used as the test article freestream conditions, are given in Table I for four of the tests (one at each nominal enthalpy). Throughout the paper, only one representative condition per nominal enthalpy is calculated, here chosen as the tests at 7.87, 13.83, and 20.83 MJ/kg. For the other tests in Table I, the reported freestream was obtained by the 1D nozzle code described in [25]. Temperatures from the 1D nozzle code are generally within 5-15% of the 2D CFD solution.

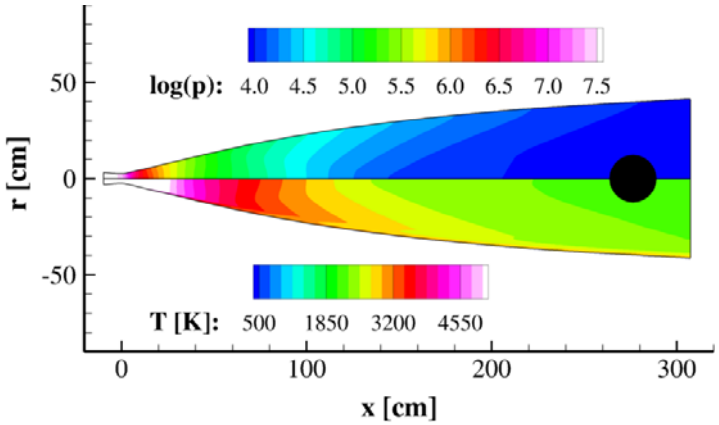

Figure 4. Sample nozzle solution (at 20.8 MJ/kg) used for computing freestream conditions.

Once the freestream conditions were extracted from the nozzle solutions, the test article simulations were run with (mostly) the same modeling assumptions as the nozzle solutions for consistency. Due to the low Reynolds numbers on the test article, however, the flowfield was solved as laminar. The probe test article solutions were run on a grid with a resolution of 192 cells in the streamwise direction and 160 cells in the wall-normal direction for a total of 30,000 cells. The initial grid was generated to extend far beyond the shock location so it could be used for multiple freestream conditions. The internal grid tailoring algorithm in DPLR was used to align the outer boundary of the grid with the shock and cluster points near the wall to resolve the boundary layer. At least three grid

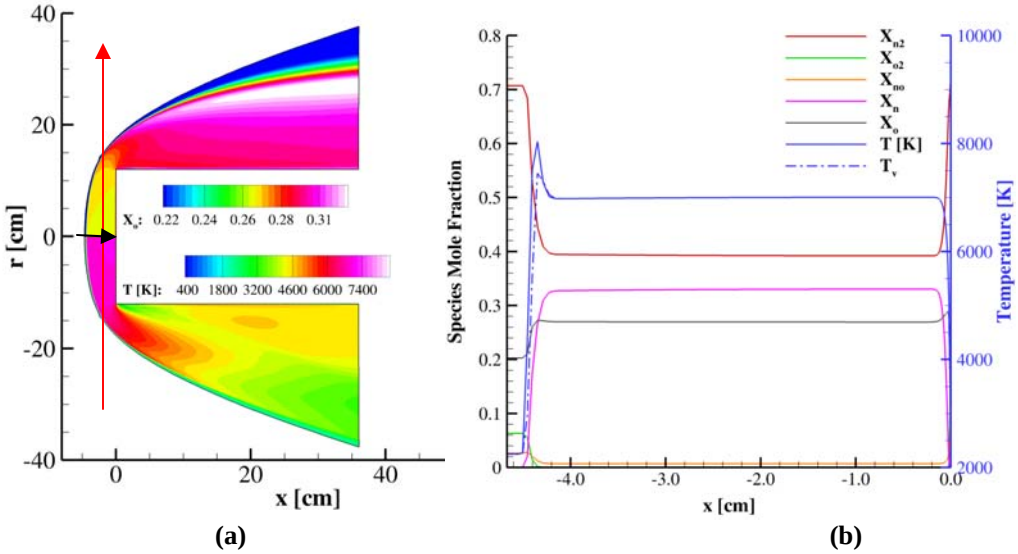

Figure 5. Sample test article solution (20.8 MJ/kg) for radiation analysis. (a) Contours of atomic oxygen mole fraction on top and translational temperature on bottom. Arrows indicate approximate line of sight extraction directions for use with NEQAIR. (b) Stagnation line temperatures and species mole fractions.

tailorings were performed to best resolve the shock layer and the steep gradients within the boundary layer. Global density residuals were tracked to measure convergence. A 2D representation of a completed solution can be found in Figure 5(a) with contours of the atomic oxygen mole fraction on top and the translational temperature on the bottom. The corresponding species mole fractions and temperatures along the stagnation line are given in Figure 5(b). Species not shown include the ionized species and electrons, which are generally less than 6×10^{-4} mole fraction. One simulation performed with a chemical equilibrium wall determined the maximum impact of catalysis to convective heating to be 0.6% and a separate simulation with turbulent flow predicted an increase of 0.2% to the convective heating, though these results were not subjected to further evaluation.

Lines of sight, extracted from the CFD solutions perpendicular to the test article, were selected at several locations between the test article and shock front and parsed into NEQAIR v14.0 [13] to calculate the magnitude of radiation in the shock layer. Cross sections perpendicular to the tube axis (red arrow) were run in line of sight mode to simulate the spectroscopic measurement, while cross-sections on the center line (black arrow) were run in stagnation point mode to obtain the radiative heat flux on the model. For the perpendicular calculation, the line of sight was extended to r = -40 to 40 cm to estimate the impact of the freestream (the characteristics of which is assumed to be the same as the core flow). NEQAIR was run with atomic lines (N and O) and molecular bands (NO, O_2, and N_2) enabled. The solution included both bound-bound and bound-free atomic features. Cases run with both quasi-steady state (QSS) and Boltzmann distributions were found to be nearly identical. For the current work, the capabilities of NEQAIR were extended to include iron bound-bound transitions. The bound-bound transitions were obtained from the NIST atomic spectral database [26] and included only lines with reported Einstein A-coefficients. This corresponds to 2,542 lines and 846 states. (An additional ~7500 lines without Einstein A coefficients are omitted, but these are presumed to be weak.) A QSS model for iron was not implemented. Bound-free rates were also implemented in NEQAIR based on the photoionization cross-sections of Bautista [27], which follows the TOPBase format [28]. To test the impact of the bound-free transitions, solutions were generated with the Fe^+ density determined from the Saha-Boltzmann relationship. In most cases, this approach would increase the charged species densities by several times, and the electron density would need to be increased to maintain charge neutrality. The effect on the NEQAIR result was not significant, so that the bound-free radiation is not included in the results reported. While the effect of iron ionization on both free-stream and shock layer characteristics could be significant, it is not computed here due to the lack of suitable rate models. On the premise that the nozzle expansion may not be predicted properly for this and other reasons [2], adjustments were also made to the freestream vibrational/electronic temperature and NO fraction in order to better match the experimental data. These adjustments would impact only the line of sight spectral signature and not the stagnation point heating magnitude.

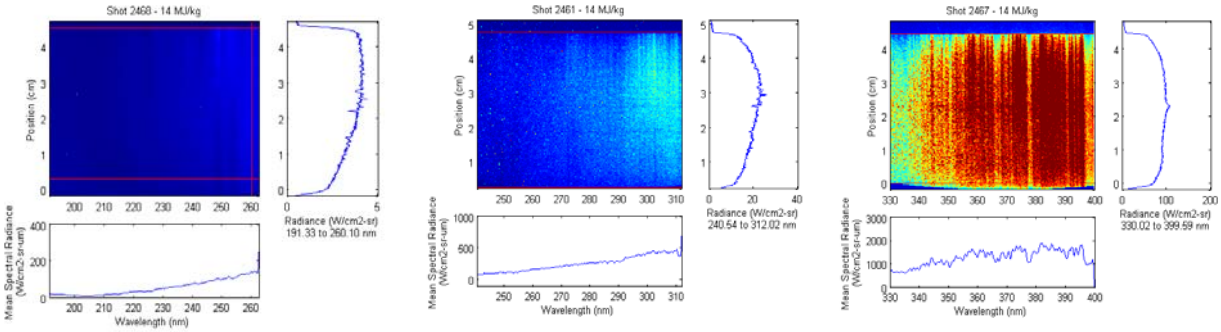

Figure 6. Spectroscopic measurements at 14 MJ/kg condition. The y-axis represent distance from the model face (y = 0 is surface), while the x-axis is the wavelength measured in nm. Images represent spectral ranges from (a) 190-260 nm, (b) 240-310 nm, (c) 330-400 nm.

IV. Results

Data are obtained in the form of three dimensional images of spectral radiance as a function of position and wavelength. Three such images are shown in Figure 6 for the 14 MJ/kg condition. The test article is at the bottom of the image, and the shock front can be seen at approximately 4.5 cm from the test article. The spatial profile of radiance within the shock is apparent from the vertical cross sections in each sub figure, while spectral profiles are given in the horizontal cross-sections. The spatial dependence is fairly gradual – no significant non-equilibrium overshoot is apparent at the shock front. This is partially due to the optical imaging volume being up to 1.2 cm in diameter at the bow shock edge, though the DPLR/NEQAIR predictions also show small variation over much of the shock length. Since the spatial variation is small, the remainder of the paper will discuss only the spatially averaged

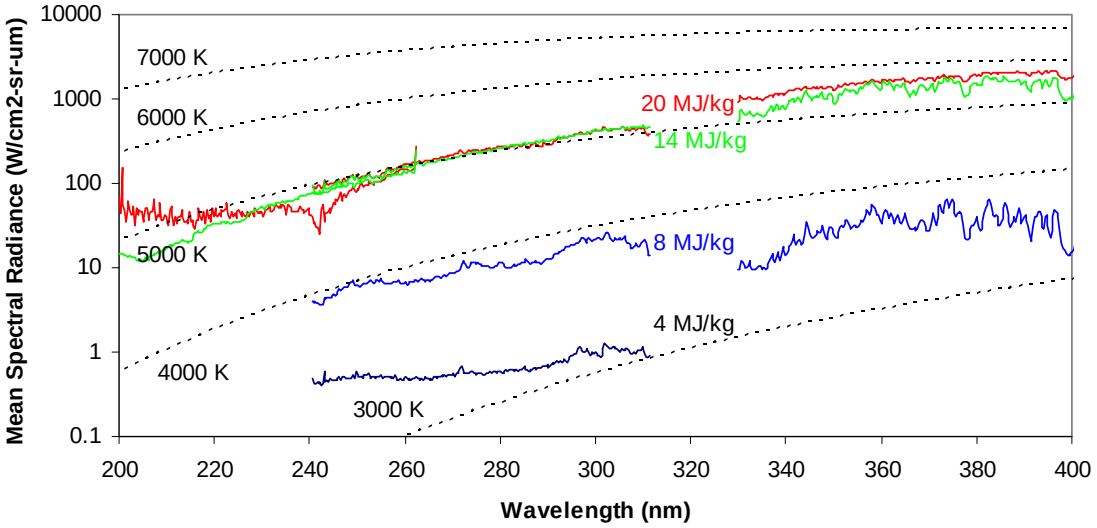

Figure 7. Summary of spectral radiance for four nominal enthalpies from 4-20 MJ/kg. Also shown are equivalent blackbody radiances at 1000K intervals.

spectra. Vertical features on the 3D images, when present, represent the contributions of various atomic or molecular transitions. Below 350 nm, few features are apparent and the radiation appears to be blackbody-like in nature. While many features are seen above 350 nm, there is no space between the features, also indicating an underlying continuum or blending of adjacent lines.

The average spectral profiles from all tests are summarized in Figure 7 on a logarithmic scale. For reference, blackbody curves at 1000K intervals are overlaid on the plot. The signal at 4 MJ/kg is fairly low with no significant features. At 8 MJ/kg, significant spectral features are observed between 300-400 nm with broader features at lower wavelength. At 14 MJ/kg, the features apparent at low enthalpy begin to become absorbed, making them less prominent and the emission more continuous in nature. Below 300 nm, the radiance is best described as a continuum and nearly follows that expected for a 5000K blackbody. The radiance at 20 MJ/kg is only slightly higher than at 14 MJ/kg and is almost entirely Planck-limited. The effective blackbody limit of this spectrum however does not follow a single temperature blackbody curve but passes between 5000-6000K as wavelength increases. This temperature is significantly less than the shock layer temperature predicted by CFD, but higher than the expected temperature outside of the shock region. The result suggests that absorbing species may be present at the shock edge or in the nozzle flow at elevated temperatures. The latter phenomenon has previously been surmised

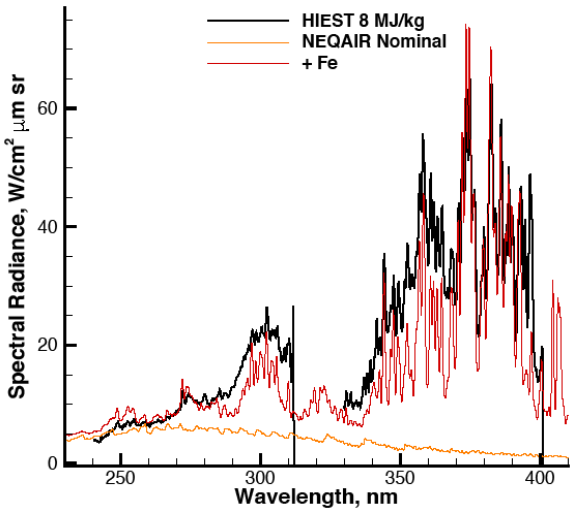

Figure 8. Composite experimental spectrum obtained from two tests at 8 MJ/kg and corresponding NEQAIR predictions. NEQAIR requires 0.3% Fe to be added to the flow to match the spectrum.

to cause mis-prediction of heating magnitudes in CO_2 tests in reflected shock tunnels.[2] The features apparent between 300-400 nm cannot be assigned to any species known to radiate in pure air shocks. However, they can be attributed to iron, carbon and other impurity atoms measured by Nomura, et al. [12] at higher wavelengths and similar shock conditions. The presence of carbon in the shock would result in the production of CN, which is known to radiate strongly near 390 nm as an impurity in air and N_2 plasmas [29, 30]. Attempts to match the individual spectra by introducing impurity species will be described in the following paragraphs.

The experimental profile for the 8 MJ/kg condition is shown in Figure 8, along with the NEQAIR predictions with and without the inclusion of iron vapor as an impurity. NEQAIR fails to predict the majority of the experimental spectrum, matching in magnitude only for wavelengths less than 250 nm, if the flow medium is assumed to be pure air. Adding Fe vapor to the NEQAIR simulations matches the structure of the spectrum qualitatively. Closer examination of the lines in the two spectra show the location of most spectral peaks and valleys to be matched exactly, confirming iron to be the major contributor to the impurity emission. Varying the mole fraction of iron, it is found that $x_{Fe} = 0.003$ gives the best match to the spectrum as shown in Figure 8. In an attempt to improve the under-predicted region, small amounts of cyanogen radical were introduced to the NEQAIR simulation. However, this tended to worsen the agreement near the band head (380-390 nm) so is not shown. Additional discrepancies between the experiment and the spectrum can be attributed to a variety of factors, including missing lines or inaccurate Einstein A coefficients from the NIST database, additional impurity sources, non-Boltzmann populations in the Fe levels, inaccuracies in the CFD temperature profile, or variations in the experimental test parameters (e.g. enthalpy differences between tests, unsteady phenomena, spatial resolution).

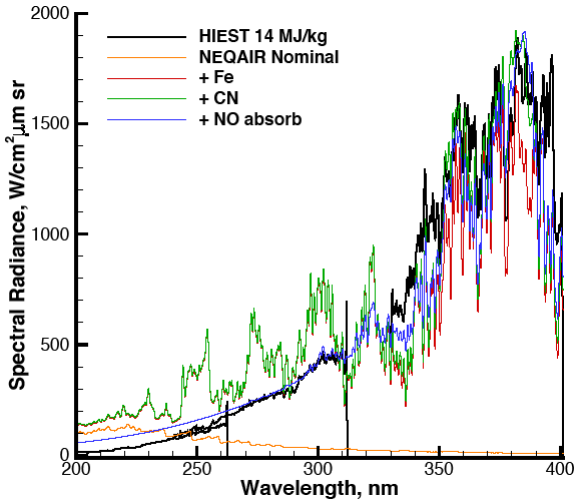

Figure 9. Composite spectrum (3 tests) at 14 MJ/kg and various NEQAIR simulations. In this case, adjustments to both impurities and the freestream are required to match the spectrum.

Figure 9 shows the 14 MJ/kg spectra with various NEQAIR fits. As with the 8 MJ/kg condition, the nominal NEQAIR simulation is inconsistent with the data. In this case, the radiance is overpredicted below 250 nm and underpredicted above 250 nm. In order to match the spectrum from 350-400 nm, it was necessary to introduce an Fe mole fraction of at least 0.03 (red curve). In this case, much of the iron radiation is self-absorbed so that further increasing the iron fraction results in smaller increases in radiance and good fits may still be obtained with a much larger iron fraction. The inclusion of CN at 2×10^{-3} fraction (green curve) improves the fit without requiring further increase to Fe fraction. The introduction of Fe radiation also increases the overprediction at low wavelength. The portion of the curve from 200-300 nm closely resembles a blackbody near 5000 K. This is lower than the shock layer temperature of 6000 K, so suggests that the radiation is absorbed outside of the shock in the freestream. The freestream temperature, however, is only about 1600K and does not contribute sufficient absorbance by itself. As discussed above, it has been previously postulated that vibrational relaxation in an expanding flow may be incomplete and inaccurately predicted by CFD codes [2]. Therefore the vibronic temperature in the freestream has been increased to match the spectrum. At the same time, species that absorb in the range of 200-300 nm, but not 350-400 nm, need to be introduced into the freestream to produce sufficient absorption. For the blue curve in Figure 9, the freestream NO fraction is increased with the temperature until the absorption level reasonably matches experiment. The amount of NO required is larger than the freestream density predicted at this point in the flow, so that this cannot be the actual mechanism for the absorption. This may suggest that there is additional NO or other

absorbing species in the cooler edge regions of the shock layer. An alternative explanation may be that additional impurities are present in the freestream. Assuming the maximum impurity density to be 10^{17} cm^{-3} over the 25 cm section of nozzle flow, an absorption cross-section larger than 2×10^{-18} cm^2 is needed to match the data.

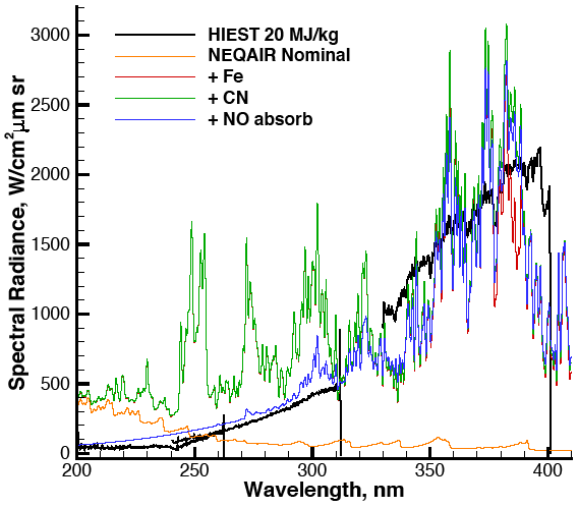

Figure 10. Radiance measured at 20 MJ/kg and corresponding NEQAIR fits.

Figure 10 shows the radiance measurements at 20 MJ/kg in comparison to the NEQAIR fits. Similar to the 14 MJ/kg case, the nominal NEQAIR simulation overpredicts the radiance below 250 nm and underpredicts above 250 nm. This indicates again that both iron and CN contamination and freestream absorption are present. The amount of Fe required is comparable to the 8 MJ/kg case at 0.003 mole fraction (red curve). Though the magnitude of the radiance is matched, the shape is poorly predicted. Inclusion of CN at a 10^{-4} level (green curve) improves the agreement though there are still some unpredicted gaps in the spectrum. The radiance in this region appears to be optically thick with an effective temperature near 5500K. However, this temperature would be too large to match the low wavelength radiance and too low for the shock layer temperature. The region below 300 nm is reasonably matched by increasing the freestream temperature to 5000 K. The changing blackbody character of the radiance suggests other complex phenomenon that we are presently unable to reproduce. This may relate to additional absorbing impurities or the temperature profile in the non-equilibrium shock region.

Table II. Parameters used to fit experimental spectra

Enthalpy (MJ/kg)	x_{Fe}	x_{CN}	T_{free} (K)	n_{NO} (cm^{-3})
8	0.003	--	--	--
14	0.03	2×10^{-3}	5000	3.6×10^{19}
20	0.003	1×10^{-4}	5000	2.7×10^{19}

A summary of the parameters used to match the radiance profiles in the three nominal conditions are given in Table II. All three conditions are relatively well matched using an iron mole fraction between 0.003-0.03 in the shock layer and CN impurity levels on the order of 10^{-3}-10^{-4}. The iron fractions reported here agree reasonably well with those reported by Nomura, et al. [12], though the CN level was not measured in their work. For the 14 MJ/kg and 20 MJ/kg case, it was necessary to both increase the freestream temperature and introduce absorbing species in order to match the lower level of radiation observed below 300 nm. The vibronic temperatures were increased to 5000 K for both cases. The iron and CN contamination in the expanded cross-sectional freestream were set to negligibly small values while large concentrations of NO were introduced to cause absorption. Though the spectra obtained mostly match the observations, the spectra are not unique solutions. The self-absorption of radiance in the shock layer makes the radiance relatively insensitive to iron mole fraction at high levels of impurity. To some extent, addition of CN to the shock layer can compensate the level of iron required. CN by itself (or at large fraction) would not match the features well, however. The varying level of blackbody limited radiance suggests the absorption to be occurring by different species over a range of temperatures. One possibility is that the absorption is occurring in the non-equilibrium zone over the line of sight. The non-equilibrium zone corresponds to where the

bow shock is curving around the model and displays a non-equilibrium overshoot. The accuracy of both the CFD and QSS/Boltzmann prediction in this regime may have significant impact on the radiance observed. To demonstrate the effect of this region, both the temperature profiles and the accumulated line of sight radiance from 200-400 nm are displayed in Figure 11. The temperature contours in Figure 11(a) display a drop from the core temperature beginning at a radius of ~10 cm. This downward temperature trend briefly reverses at the shock edge before sharply falling to the freestream temperature. The accumulated line of sight radiance (Figure 11(b)) increases steadily through most of the shock layer. At 14 and 20 MJ/kg, some curvature is apparent as portions of the spectrum become optically thick. The maximum radiance is obtained near the 10 cm location where the temperature trend reverses. This indicates that absorbance is occurring in this cooler region, therefore the final spectrum obtained will be sensitive to how well this region is predicted. Further attempts to better understand the spectra will likely need to focus in this region. The absorption and emission occurring in the freestream (i.e. r > ~15 cm) is a result of our adjustment of NO mole fraction, and may not be required were the non-equilibrium zone predicted differently.

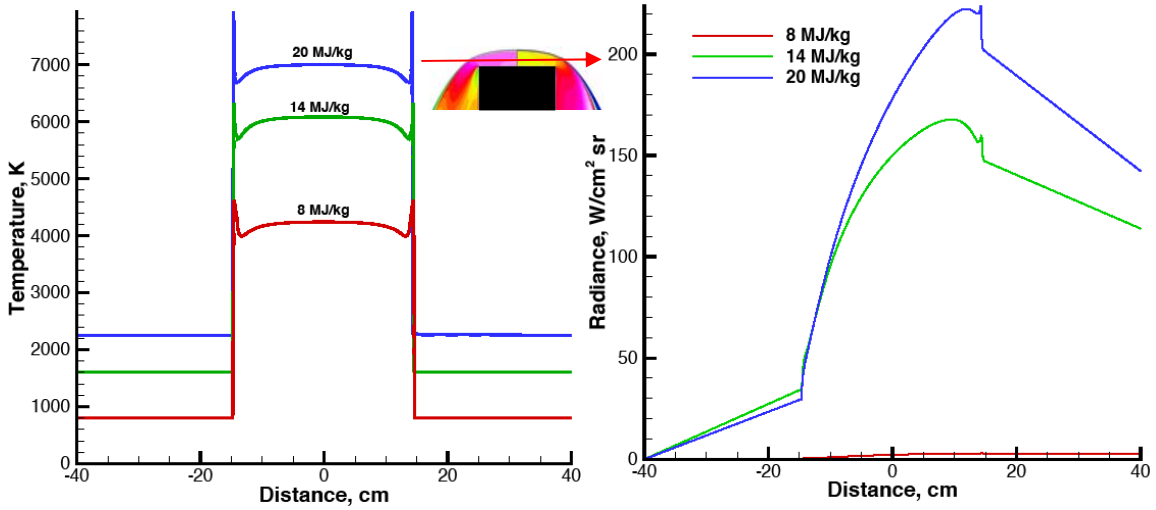

Figure 11. Plots showing (a) the temperature contours along the radial direction for the three nominal test conditions and (b) the accumulated line of sight radiance calculated by NEQAIR for the three cases. The inset shows the orientation of the line of sight.

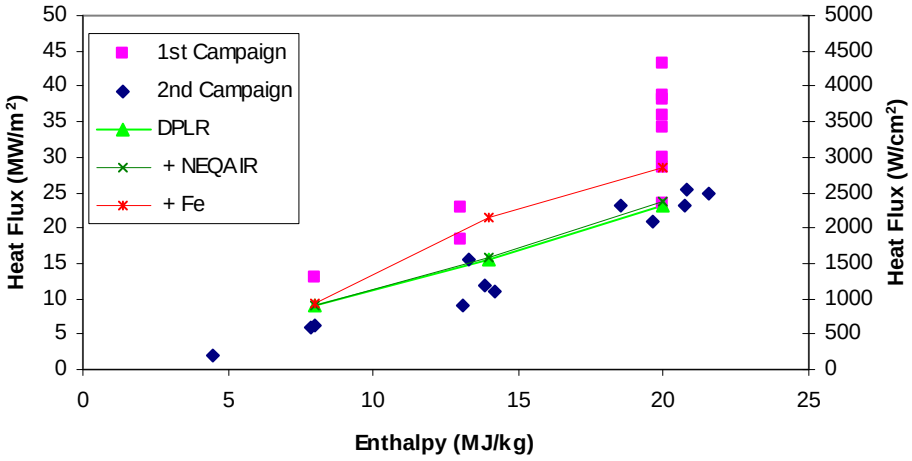

Figure 12. Heat fluxes measured in HIEST and predicted by DPLR and DPLR+NEQAIR.

To test the hypothesis that the heating augmentation factor is caused by radiation, the adjusted impurity levels are added to the nominal convective heating as calculated by DPLR along the stagnation line and evaluated with the stagnation heating (i.e. tangent slab) option in NEQAIR. This result will only be sensitive to the iron and CN level adjusted to match the spectra, as any absorption introduced to the freestream does not impact the stagnation line of

sight. Since the iron and CN were introduced at near the minimum level required to match the observed spectra, the result should represent a lower bound to the actual radiative heating on the stagnation line. Figure 12 contains the experimentally measured heating values across two campaigns in HIEST. The first campaign corresponds to measurements made in Ref [11] without the use of a blocking window, while the data from the current campaign utilizes reflective thermocouples which were expected to not measure the radiative heating component. The nominal convective heating values from DPLR are shown as a connected green line in Figure 12 and agree well with the current data set. The inclusion of the nominal NEQAIR radiative heating makes a minimal impact of the DPLR value, increasing it by no more than 2%. With the Fe and CN impurity introduced to the freestream, the total heat flux increases by between 10-590 W/cm^2, which brings it closer in line with heat fluxes measured in the first test series. It is probable that the impurity level is not reproducible between tests, thus the scatter in the data may be caused by variations in the impurity. Therefore the radiation predicted in this work would only apply to the particular tests for which spectra were collected. That the predictions here are consistent with the lower end of the data supports the idea that impurity radiation is responsible for much, if not all, of the heating augmentation. The spectral radiance along the stagnation line of sight is shown in Figure 13. It is apparent that the majority of radiation (between 53-67%) originates from the 200-400 nm region measured in this work, though there is also significant contribution (29-46%) above 400 nm. Unlike the spectra observed perpendicular to the model, there is no strong blackbody absorption predicted above 200 nm. This is because the boundary layer around the model is much thinner than the width of the nozzle flow. The spectrum is consistent with Ref. [11] which deduced that the majority of heating (greater than 77% in this work) originates above 300 nm with a smaller contribution from lower wavelengths.

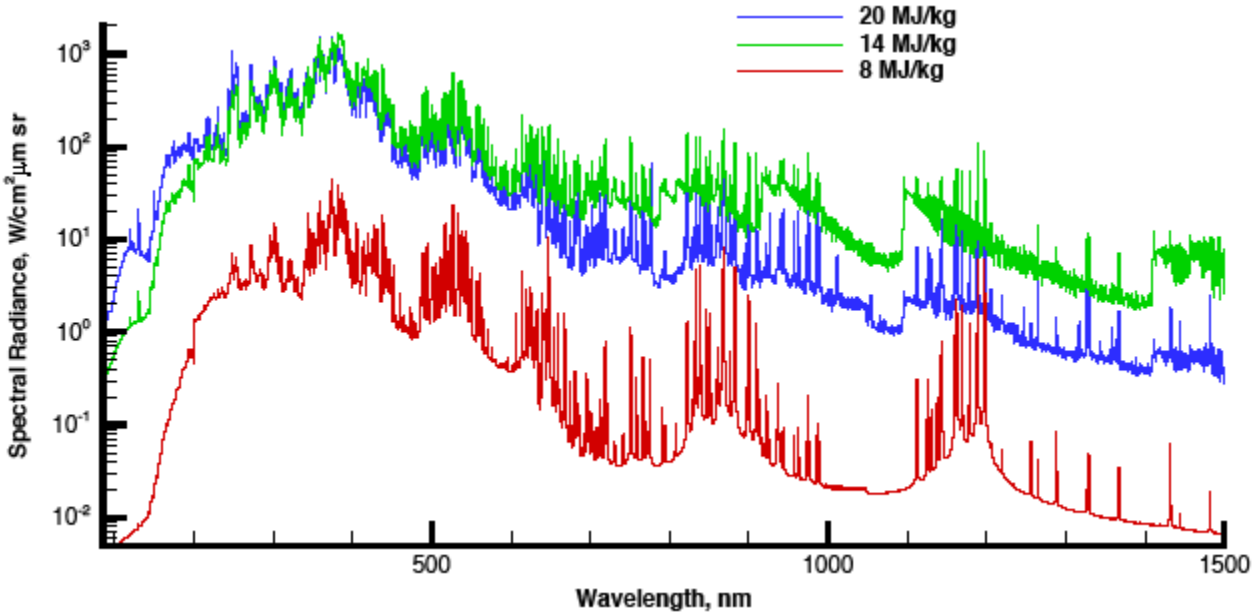

Figure 13. Spectral radiance predicted on the stagnation line

Conclusions

This paper has presented a characterization of radiance across a model in the HIEST reflected shock tunnel facility. The spectra from 200-400 nm are measured over several tests at nominal enthalpy levels of 4, 8, 14 and 20 MJ/kg. The spectrum obtained are spatially resolved along the tube axis and integrated along the line of sight perpendicular to the tube. The spectra display levels of radiation that are inconsistent with predicted radiative profiles from the DPLR CFD code and NEQAIR radiation software. It is shown that addition of iron contaminants between 0.003-0.03 mole fraction explain the majority of unexpected radiation. At higher enthalpies, the radiation displays a blackbody limit between 5000-6000 K which is inconsistent with both the predicted free nozzle flow and bow shock temperatures. An attempt to fit the spectrum was made by increasing the vibronic temperature in the nozzle flow and increasing the NO fraction. Satisfactory fits to the spectra were obtained, though it is expected that the physics are not captured correctly by these adjustments. It is speculated that additional absorbing impurities are present and that the non-equilibrium zone where the shock curves around the model is predicted incorrectly. The

fact that the radiance accumulated over the line of sight reaches a maximum at the beginning of the shock non-equilibrium zone gives credence to the idea that the blackbody limits occur in this region.

The impurity levels required to match the spectra observed normal to the shock axis were used to calculate the equivalent radiance and radiative heating incident on the model stagnation point. This calculation would not be sensitive to the freestream absorbance process but instead is only sensitive to the amount of impurity introduced. It was surmised that the impurity level would be a lower bound as the blackbody limits of absorbance preclude determining an upper bound at the highest enthalpy cases. The equivalent radiative heating predicted at the stagnation point was as large as 590 W/cm^2 which matches the lower bound of the observed heating augmentation. It is expected that the impurity level may vary between tests such that a range of augmentations may be observed on different tests. On this basis, there is strong evidence that most, if not all, of the heating augmentation comes from impurity radiation. The impurity radiation is expected to decrease at lower enthalpies and for smaller models as the shock layer temperatures and shock stand-off distances, respectively, decrease.

While this evidence, in addition to that reported in Refs. [11, 12], very strongly support the radiative heating hypothesis, additional work is desired to better understand the mechanism. That the absorption is poorly predicted suggests improvements in the computational approach and better understanding of the impurity species should be explored. Additionally, spectral measurements from the model face out into the shock layer, which would not be obscured by absorbing free-stream species, is highly desirable to better quantify the shock layer radiation and heating. By improving the understanding of the tunnel radiative heating, it may be possible to provide better physical understanding of test results and improve predictive tools and model validation through ground-based hypersonic tests.

Acknowledgments

The authors would like to thank NASA's MPCV Aerosciences Program, Entry Systems Modeling (ESM) project and Thermophysics Facility Branch for their support of this work. Drs. Brett Cruden and Aaron Brandis are supported through the NNA10DE12C contract between NASA Ames Research Center and ERC Inc.

References

1. Hollis, B. R., and Prabhu, D. K., "Assessment of Laminar, Convective Aeroheating Prediction Uncertainties for Mars-Entry Vehicles," *Journal of Spacecraft and Rockets,* Vol. 50, No. 1, 2013, pp. 56-68.
2. MacLean, M., and Holden, M., "Numerical Assessment of Data in Catalytic and Transitional Flows for Martian Entry," AIAA Paper 2006-2946.
3. Tanno, H., Komuro, T., Sato, K., Itoh, K., Takahashi, M., Ishihara, T., Ogino, Y., and Sawada, K., "Heat Flux anomaly in high-enthalpy and high Reynolds number flow," AIAA Paper 2012-3104.
4. Olejniczak, J., Wright, M., Laurence, S., and Hornung, H., "Computational Modeling of T5 Laminar and Turbulent Heating Data on Blunt Cones, Part 1: Titan Applications," 2005.
5. Hollis, B., Liechty, D., Wright, M., Holden, M., Wadhams, T., MacLean, M., and Dyakonov, A., "Transition Onset and Turbulent Heating Measurements for the Mars Science Laboratory Entry Vehicle," 2005.
6. Marineau, E., Laurence, S., and Hornung, H., "Apollo-Shaped Capsule Boundary Layer Transition at High-Enthalpy in T5," 2010.
7. Marineau, E., Lewis, D., Smith, M., Lafferty, J., White, M., and Amar, A., "Investigation of Hypersonic Laminar Heating Augmentation in the Stagnation Region," 2013.
8. Holden, M., Duryea, G., Gustafson, G., and Hudack, L., "An experimental study of particle-induced convective heating augmentation," 1976.
9. Bogdanoff, D. W., and Park, C., "Radiative interaction between driver and driven gases in an arc-driven shock tube," *Shock Waves,* Vol. 12, No. 3, 2002, pp. 205-214.
10. Ishihara, T., Yousuke, O., Ohnishi, N., Sawada, K., and Tanno, H., "Numerical Study on Anomalous Heating over Blunt-body in Free-Piston Shock Tunnel HIEST," AIAA Paper 2013-0909.
11. Tanno, H., Komuro, T., Ohnishi, N., Ishihara, T., Ogino, Y., and Sawada, K., "Experimental Study on Heat Flux Augmentation in High-Enthalpy Shock Tunnles," AIAA Paper 2014-2548.
12. Nomura, S., Takayanagi, H., Fujita, K., Tanno, H., Komuro, T., and Itoh, K., "Spectroscopic Investigation on Anomalous Heating in Free Piston Shock Tunnel HIEST," AIAA Paper 2014-2545.
13. Cruden , B. A., and Brandis, A. M., "Updates to the NEQAIR Radiation Solver," *Radiation in High Temperature Gases*. St. Andrews, UK, 2014.
14. Itoh, K., Ueda, S., Tanno, H., Komuro, T., and Sato, K., "Hypersonic aerothermodynamic and scramjet research using high enthalpy shock tunnel," *Shock Waves,* Vol. 12, No. 2, 2002, pp. 93-98.

15. Tanno, H., Komuro, T., Sato, K., Itoh, K., Yamada, T., Sato, N., and Nakano, E., "Heat flux measurement of Apollo capsule model in the free-piston shock tunnel HIEST," AIAA Paper 2009-7304.
16. Prabhu, R., and Erickson, W. D., "A rapid method for the computation of equilibrium chemical composition of air to 15000 K," NASA TP-2792, 1988.
17. Greenberg, R. B., Cruden, B. A., Grinstead, J. H., and Yeung, D., "Collection optics for imaging spectroscopy of an electric arc shock tube," *Proccedings of the SPIE, Novel Optical Systems Design and Optimization XII*. Vol. 7429, 2009, 74290H.
18. Wright, M. J., Candler, G., and Bose, D., "Data-Parallel Line Relaxation method for the Navier-Stokes Equations," *AIAA Journal,* Vol. 36, No. 9, 1998, pp. 1603-1609.
19. Gupta, R. N., Yos, J. M., Thompson, R. A., and Lee, K. P., "A Review of Reaction Rates and Thermodynamic and Transport Properties for an 11-Species Air Model for Chemical and Thermal Nonequilibrium Calculations to 30000 K," NASA RP-1232, 1990.
20. Yos, J. M., "Transport properties of nitrogen, hydrogen, oxygen, and air to 30,000 K," TR AD-TM-63-7, Avco Corp., March 1963.
21. Ramshaw, J. D., "Self-consistent effective binary diffusion in multicomponent gas mixtures," *Journal of Non-Equilibrium Thermodynamics,* Vol. 15, No. 3, 1990, pp. 295-300.
22. McBride, B. J., and Gordon, S., "Computer program for calculation of complex chemical equilibrium compositions and applications II. User's Manual and Program Description," NASA RP-1311-P2, June 1996.
23. Menter, F. R., "Two-equation eddy-viscosity turbulence models for engineering applications," *AIAA Journal,* Vol. 32, No. 8, 1994, pp. 1598-1605.
24. Spalart, P. R., and Allmaras, S. R., "A one-equation turbulence model for aerodynamic flows," AIAA Paper 92-0439.
25. Takahashi, M., Kodera, M., Itoh, K., Komuro, T., Sato, K., and Tanno, H., "Influence of thermal non-equilibrium on nozzle flow condition of high enthalpy shock tunnel HIEST," AIAA Paper 2009-7267.
26. "NIST Atomic Spectra Database." Vol. 2011, 2015.
27. Bautista, M. A., "Atomic Data from the IRON Project. XX. Photoionization cross sections and oscillator strengths for Fe I," *Astron Astrophys Suppl Ser,* Vol. 122, 1997, pp. 167-176.
28. Cunto, W., Mendoza, C., Ochsenbein, F., and Zeippen, C., "TOPbase at the CDS," *The Opacity Project: Selected research papers-Atomic Data Tables for S to Fe,* Vol. 2, 1994, p. 53.
29. Cruden, B. A., Martinez, R., Grinstead, J. H., and Olejniczak, J., "Simultaneous Vacuum Ultraviolet through Near IR Absolute Radiation Measurement with Spatiotemporal Resolution in an Electric Arc Shock Tube," *41st AIAA Thermophysics Conference*. AIAA, San Antonio, TX, 2009, AIAA 2009-4240.
30. Grinstead, J. H., Wilder, M. C., Olejniczak, J., Bogdanoff, D. W., Allen, G. A., Dang, K., and Forrest, M. J., "Shock-heated Air Radiation Measurements at Lunar Return Conditions," *46th AIAA Aerospace Sciences Meeting*. AIAA, Reno, Nevada, 2008, AIAA 2008-1244.